A Deep Look into Dynamics of Saltwater Imbibition in a Calcite Nano-Channel: Temperature Impacts Capillarity Regimes

Mohammad Hasan Badizad[1, †], Mohammad Mehdi Koleini[2, ‡], Hugh Christopher Greenwell[3],

Shahab Ayatollahi[2, *], Mohammad Hossein Ghazanfari[1]

[1] Department of Chemical and Petroleum Engineering, Sharif University of Technology, Tehran, Iran.
[2] Sharif Upstream Petroleum Research Institute (SUPRI), Department of Chemical and Petroleum Engineering, Sharif University of Technology, Tehran, Iran.
[3] Department of Earth Sciences, Durham University, Durham, DH1 3LE, UK
† **Email:** mohammadhasan.badizad@che.sharif.edu & badizad@gmail.com
‡ **Email:** mmkoleini@che.sharif.edu & mmkoleini@gmail.com
*Corresponding Author; **Email:** shahab@sharif.edu & dr.ayatollahi@gmail.com

Abstract

This research concerns fundamentals of spontaneous transport of saltwater (1 mol.dm^{-3} NaCl solution) in nano-pores of calcium carbonates. A fully atomistic model was adopted to scrutinize temperature-dependence of flow regimes during solution transport under $CaCO_3$ nano-confinement. The early time of capillary filling is inertia-dominated and solution penetrates with a near planar meniscus at constant velocity. Following a transition period, the meniscus angle falls to a stabilized value, characterizing the capillary-viscous advancement in the calcite channel. At this stage, brine displacement follows a parabolic relationship consistent with classical Lucas-Washburn (LW) theory. Approaching the slit outlet, the meniscus contact lines spread widely on the solid substrate and brine leaves the channel at constant rate, in oppose to LW law. The brine imbibition rate considerably increases at higher temperatures, as a result of lower viscosity and greater tendency to form wetting layers on slit walls. We also pointed out longer primary inertial regime as well as delayed onset of the viscous-capillary regime at higher temperature. Throughout the whole span of capillary displacement, transport of sodium and chloride ions is tied to dynamics and diffusion of the water phase, even at the mineral interface. The results presented in this study are of broad implications in diverse science and technological applications.

Keywords: Capillary; Confinement; Calcite; Imbibition; Molecular dynamics simulation; NaCl; Brine; Temperature.

Introduction

Fluid flow in nano-scale geometries is a phenomenon of broad interest in various scientific and industrial disciplines [1]; for instance, seawater desalination using membranes, hydrocarbon flow in the subsurface formations, water uptake in concrete pores, fabrication of nano-devices and disposal of nuclear wastes [2–4]. In hydrology, underground water seeps from aquifers to overlaying unsaturated zones in a natural process induced by capillary suction in order to fill in fine pores of subsurface strata [5]. It is important to understand the capillary rise of saltwater in underground soil beds in order to evaluate the impact of human activities on water resources, *e.g.*, exploiting geothermal energy [6]. Besides soil physics, capillarity is the key mechanism in oil and gas production by injecting saline solutions into fine pores of consolidated rocks constituting petroleum reservoirs [7].

It remains challenging to experimentally probe fluid transport in porous media at nano-scale resolution [8]. Owing to the extremely large surface-to-volume ratio at nanoscopic confinements, surface forces dominantly contribute to fluid transport in such media [9]. On the other hand, the granularity, *i.e.*, discrete nature, of constituting species becomes important in narrow spaces and a fluid may behave differently from a continuum expectation [10]. Concerning these matters, molecular dynamics (MD) simulations have been widely utilized for interpreting and complementing empirical observations [11]. It is a promising tool for exploring fundamentals of fluid flow within tight pores, where classical fluid dynamics theory fails to give an accurate picture [12]. To date, MD simulation has been employed in diverse research areas for scrutinizing solid-liquid interfaces in atomic details [13].

Zambrano and co-workers pointed out the anomalous dynamics of imbibition water imbibition in silica nano-pores, not exactly complying with well-established microfluidics theories [14–16]. Later studies probed the influence of pore shape and also influence of imposing an external electrical field on water imbibition inside silica channels [17]. In the context of brine imbibition in cementitious materials, Hou et al. carried out a theoretical study on the migration of ions

contained in NaCl and Na_2SO_4 solutions in calcium-silicate-hydrate (CSH) slits [18]. Further, Wang et al. explored capillary adsorption of cesium chloride in CSH to assess durability of that substance upon exposure to aqueous environments [19]. MD simulation has also been used to gain insight into the molecular mechanism behind oil mobilization by injecting nanoparticles in silica rocks [20]. He and co-workers analyzed imbibition strength of water augmented by nanoparticles for displacing polar and apolar oils confined within silica and synthetic nano-pores [20–22].

Despite numerous experimental and numerical studies conducted so far, yet structure and dynamics of saline solutions imbibing into nano-confinements are not completely understood, in particular little is known about carbonates. Calcite is the most abundant carbonate mineral, majorly found in ultratight hydrocarbon-bearing formations, subsurface cap rocks and vadose zones [23,24]. Besides, $CaCO_3$ takes an important role in biology, *e.g.*, as a bone substitute or coral skeleton [25,26]. However, there is a paucity of research on the capillary uptake into calcite nano-pores. Motivated by this knowledge gap, we explored for the first time the spontaneous transport of saltwater in a calcite nano-slit by applying atomistic simulation. The imbibing fluid was represented by 1 $mol.dm^{-3}$ NaCl solution in accordance with typical salinity of marine and aquifer environments [27]. As a further novelty of this research, we scrutinized flow regimes of brine imbibition in the hydrophilic nano-confinement in a range of temperatures, namely, 300, 330 and 360 K. In the remainder of this paper, we will concisely explain the simulation procedure and then provide an in-depth analysis on the dynamics and structural properties of water and ions within the calcite channel. Finally, we will end up with some concluding remarks.

Simulation protocol

Model construction

Spontaneous capillarity (*i.e.*, capillary flow not driven by any external force like gravity or pressure drop) was modeled by an 18 nm-long slit, which was constructed by placing two parallel calcite slabs 6 nm apart in the z-direction (**Figure 1**). The chosen slit spacing is in accord with the typical pore size encountered in nature and industrial applications, such as shale reservoirs, cementitious materials and nano-devices [19,28–30]. Each slab was composed of 14 calcium carbonate layers (~4.1 nm-thick) with areal dimensions of 5.8 × 18 nm^2 ($L_x \times L_y$) Calcite $(10\bar{1}4)$ cleavage plane is the most stable and abundant polymorph of $CaCO_3$ mineral in the nature [31], so that it was chosen to model slit walls. NaCl solution of salinity 1 $mol.dm^{-3}$ represents imbibing saltwater in this study. The brine was constructed by randomly filling a 5.8 × 12.5 × 14 nm^3 orthorhombic box with 30653 water molecules and 552 Na^+ and Cl^- ion pairs using Packmol program [32]. Initially, the solution was relaxed at the desired temperature, (300, 330 or 360)K, and then was placed next to the channel entrance. Hou et al. carried out a same procedure for simulating transport of saline solutions inside a CSH nano-pores [18]. Following suggestion by Wang et al. [19], boundary effect was avoided by creating two 10 nm-thick vacuum spaces beside the slit's outlet and the aqueous solution by elongating the simulation box in the y-direction (slit axis). Furthermore, two invisible hard walls were set at the end side of those gaps to prevent water molecules flying out, as performed in relevant investigations [20,33].

Simulation details

All molecular simulations were carried out using the LAMMPS package [34], which is an efficient, general purpose program for conducting atomic-based simulations. The calcite slabs were modeled by the potential developed by Xiao et al [35]. In keeping with the parameterization procedure followed for deriving the calcite force-field, water molecules were described by

TIP3P model [36]. Sodium and chloride ions were treated as fully ionized atoms, *i.e.*, carrying charge valances 1+ and 1-, respectively, interacting through Coulombic and Lennard-Jones (LJ) potentials adopted from Joung et al.[37]. Short-range non-bonded interactions were evaluated using 12-6 Lennard-Jones potential within the cut-off radius of 1.0 nm. Long-range electrostatic Coulombic interactions were resolved by particle-particle particle-mesh (PPPM) approach with the convergence tolerance of 10^{-5}. Newton's equation of motion was integrated for each atom at discrete time steps of 1.0 fs using the velocity-Verlet scheme [38]. The trajectory (spatial coordinates and velocities) of all atoms were extracted every 200 fs for post-analysis.

Throughout the simulations, calcium and carbon atoms of calcite slabs were spatially constrained to avoid distortion or deformation of the slits walls. This practice is justified on the basis of thermodynamic and kinetic characteristics of $CaCO_3$. Calcite is a barely soluble mineral and very slowly dissolves in water [39–41]. Also, by employing amplitude modulation AFM, Ricci et al. pointed out the smooth nano-surface of $CaCO_3$ contacting aqueous solutions [42]. The choice of constrained calcite surfaces is verified by a complementary simulation, detailed in section S1 of Supporting Information (SI). In sum, the present results can be applied with confidence to real cases. Since our focus is on the dynamics of capillary flow, dimensions of calcite slabs were kept constant at different temperature (not accounting for thermal expansion/contraction). At first, an invisible wall was set at the slit's entrance to prevent waters and ions from entering into the interlayer space. Then, the brine solution was equilibrated in NVT (constant particle, volume and temperature) ensemble for 2 ns by coupling to a Berendsen thermostat with a damping constant of 0.1 ps to attain the desired temperature (either 300, 330 or 360 K). The chosen range of temperature covers typical conditions encountered in various areas of scientific and applied research, such as geology, reservoir engineering, ceramic industry, building materials, geothermal operations and biological processes [43–45]. Next, the repulsive wall was removed and simulation was

progressed at the same temperature, controlled by Nosè-Hoover thermostat until the brine fully traverses the nano-channel. Throughout, temperature of the calcite walls was adjusted by allowing oxygen atoms of carbonates to freely vibrate in response to a temperature same as that of the imbibing solution.

Results

Advancing frontier of water and ions

As shown by snapshots in **Figure 2**, the brine solution advances in the calcite channel by developing a crescent-shape front, much like what is intuitively experienced upon inserting a capillary tube in a liquid [46]. It was observed that water molecules migrate into the slit space by gradually adsorbing on the calcite walls and filling the vacancy. Meanwhile, sodium and chloride ions are carried by water molecules advancing through the pore. By comparing system's configurations at different timeframes, it is clear that the advancing meniscus gradually evolves while brine advances within the calcite slit pore. Meniscus appears almost planar at the entrance area and then gradually curves towards the pore outlet. Noteworthy, the brine solution advances faster at higher temperatures**.**

For a quantitative description, solution frontier was tracked during imbibition, presented as penetration length *vs* time in **Figure 3**. The location of brine frontier at any moment was determined following a workflow proposed on the basis of Gibbs dividing line (detailed in section S2 of SI) [47]. Meniscus location is defined as the axial (Y) coordinate where density distribution profile of the intruding brine attains half of the mean water density inside the penetrated space, which is graphically illustrated in **Figure S3**. It can be seen that the brine displacement in the slit (**Figure 3**) approximately follows a parabolic relationship, in accordance with the classical Lucas-Washburn (LW) theory [48]. In this model, the imbibition length due to capillary action is a function of the square root of time. It is also clear in **Figure**

3 that the rate of brine imbibition, *i.e.*, the slope of the penetration curve, steadily decreases while solution traverses in the channel [49]. Although displacement diagrams appear parabolic on the whole, two nearly linear parts are distinguishable, one at the very beginning and one at the late stage of water transport, as identified in **Figure 3**. It means the brine moves at constant velocity while entering into and leaving the calcite slit. Based on the snapshots taken at each stage, insets of **Figure 3**, one may think of a piston-like flow at the entrance area of the pore, whereas the brine movement at the pore outlet is driven in effect by creeping of the meniscus margins on the exterior edges and corners of calcite slabs. Hence, capillary flow at the pore outlet does not comply with the classical $\sqrt{\mathrm{time}}$-law of LW theory. The slit outlet can be thought of as the junction of pore body-throat in a typical porous network.

As can be seen in the displacement curves (**Figure 3**), the rate of capillary flow within the calcite slit is noticeably temperature-sensitive, with fastest water transport at highest temperature, 360 K. However, the water displacement does not vary linearly with the temperature, as inferred by the displacement curve at 330 K being closer to that of 360 K. As shown by tangent lines in **Figure 3**, the hotter solution intrudes faster into the slit. Moreover, the constant velocity flow at the pore entrance persists in proportion to the brine temperature, lasting up to 1.8, 2.7, and 3.6 nm from the pore entrance at 300, 330, and 360 K, respectively. On the contrary, the incipit and length over which the brine displacement is affected by the pore outlet seem temperature-independent. Notably, all displacement diagrams vary linearly (identified by blue rectangle in **Figure 3**) about 2 nm before the slit outlet irrespective of the temperature.

Ions transport was tracked along the calcite pore (**Figure 4)**, which is similar to the water displacement curves at corresponding temperatures (**Figure 3)**. Evidently, ions migration in the slit is tightly coupled to the displacement of water phase, revealing faster propagation at higher temperature. Similar to the water displacement, ion transport at the inlet and outlet of the channel is subject to some peculiarities (**Figure 4)**. Notably, ions speed up once

approaching the capillary outlet, as implied by the positive curvature of the ions' displacement diagrams at the late stage of imbibition (**Figure 4)**. This accelerating movement is possibly due to the tendency of ions for adsorbing onto the exterior walls of the confining calcite slabs, shown in inset of **Figure 4**.

As seen in **Figure 4**, advancement curves of Na^+ and Cl^- closely overlap at any temperature, reflecting their synchronous migration in the capillary. This comes with equal diffusivity of those ions in a bulk NaCl solution, as experimentally verified by Mills and Lobo [50]. Therefore, the chromatographic effect *(i.e.*, the selective separation of certain constituents from a flowing solution [51]) does not occur when the NaCl solution travels through the nano-sized calcite pore. By plotting the instantaneous position of the leading edge and rear arc of the water meniscus (**Figure S4**)**,** one will notice the ions transport curves lie in between. It suggests the sodium and chloride ions constantly appear in the interfacial region of the advancing meniscus, possibly due to the favorable interactions with the calcite surface. It comes with the observation made by Koleini et al. that Na^+ ions tend to bind onto the protruding oxygen atoms on the basal plane of a calcite slab [52,53]. As a result, a positively charged layer by adsorbed sodium cations is formed on the calcite surface, which in turn draws the chloride anions towards the surface [52,54].

Mean square displacement of water and ions

Mean square displacement (MSD) is a useful measure for quantifying extent of transport due to diffusive spreading [55]. **Figure 5** exhibits MSD diagram of ions and water at different temperatures. We notice that the MSD curves of sodium and chloride ions run in parallel to that of water. This means the ions' transport through the capillary is connected with the dynamics of solvating water molecules, which was speculated earlier upon comparing displacement curves of ions and water (**Figure S4**). Concerning variation in the slope of MSD

diagrams (**Figure 5**), two diffusion stages are identified throughout the imbibition process. At early time of imbibition (<100 ps), MSD diagrams of water and ions follow a linear relationship. This stage, highlighted in purple, coincides with the constant velocity period identified by green circle in displacement diagrams (**Figure 3**). Then, MSD transits to another linear regime lasting until the end of displacement process. It is known that self-diffusivity of a species is directly proportional to slope of its MSD curve. Simply put, steeper slope of a MSD diagram means faster diffusion. With this in mind, water experiences weaker diffusion at the beginning of imbibition, although the fastest displacement of water inside the capillary happens at this period. Later, water molecular diffusion increases and at the same time, the rate of imbibition drops gradually (inferred by the slope of displacement diagram, **Figure 3**). It suggests the increasing role of molecular diffusion beyond the earliest stage of brine intrusion into the nano-slit. Although water diffusivity enhances by increasing temperature in this study (**Figure S5**), it is practically temperature-insensitive at the earliest time of water intrusion.

Meniscus thickness

The pattern of evolution of the meniscus width gives insight into the dynamics of fluid transport in a nano-confined geometry. For this purpose, the meniscus thickness was tracked during the water penetration by invoking the "90-10" criterion, whereby the meniscus thickness is defined as the separation between the positions along the slit axis where water densities are 90% and 10% of the mean bulk value [56]. As displayed in **Figure 6**, the meniscus width gradually changes as the solution moves forward in the calcite channel. In this respect, four phases are distinguished throughout the brine capillary flow, as indicated for 300 K in **Figure 6**. At Phase 1, meniscus thickness steadily decreases while water penetrates inside the slit until ~1 nm away from the pore entrance. This stage of interface evolution coincides with the constant-velocity period already recognized in the displacement *vs.* time diagram (**Figure 3**). Subsequently, at Phase 2, the meniscus thickness monotonically rises until reaching a

plateau at Phase 3 where oscillating about a constant value. The emergence of a nearly constant interface width at Phase 3 signifies the establishment of a fully developed flow regime. The persisting fluctuations arise from the discrete (non-continuum) character of the moving fluid at sub-nanometer [16,57]. Eventually, at Phase 4, the brine approaches the channel's outlet and the meniscus thickness increases immediately. It comes about by the leading edges of the water interface being drawn to the calcite outlet.

The evolution of meniscus width along the slit axis is critically connected to the brine temperature. Consistent with displacement *vs.* time data presented earlier in **Figure 3**, the flow regime particular to the early time of imbibition (Phase 1 in **Figure 6**) lasts longer at higher temperature. Likewise, the brine experiences a longer transition period at higher temperature (Phase 2 in **Figure 6**) before achieving a stable meniscus thickness. It is also noticed that capillary flow of a hotter brine is accompanied by a wider stabilized meniscus.

Dynamic contact angle

The meniscus dynamically changes while the brine penetrates in the calcite channel. Meniscus angle throughout water imbibition was obtained through the workflow described in section S5 of SI. **Figure 7** exhibits the evolution of contact angle in terms of the propagation length in the calcite slit. Much like the interfacial thickness (**Figure 6**), the variation of the brine contact angle along the channel falls into four phases, specified for 300 K in **Figure 7**. Once the solution intrudes the capillary, meniscus angle increases to *ca* 60-80^{o}, that is the largest contact angle encountered throughout the imbibition process. This happens in contrast to strongly water-favoring feature of an intact $CaCO_3$ crystal surface [58]. However, it is in accord with the decreasing interface thickness, labeled as Phase 1 in **Figure 6**. Following this stage, the meniscus angle gradually decreases throughout the brine penetration and eventually becomes stabilized around a mean value, Phase 3 in **Figure 6**. By increasing brine

temperature, the meniscus takes longer to fully develop. Notably, the meniscus comes to a smaller stabilized angle at higher temperature, with mean values 40 °, 20 °, and 8 ° at 300, 330 and 360 K, respectively. It is argued that the brine interface undergoes a transition during which the meniscus steadily develops and at the same time, the contact angle decreases until both being stabilized. Overall, there is a one-to-one relationship between the evolution of meniscus angle and thickness, with the smaller contact angle, wider the brine interface is. Eventually, meniscus angle drops to zero close to the capillary outlet at any temperature.

Local distribution of water and ions adjacent to the calcite surface

To gain further insight into the capillary transport of water and ions, the local densities of water and ions adjacent to calcite walls were analyzed (**Figure 8**), using atomic trajectories collected during the stabilized flow (Phase 3 in **Figures 6-7**). Distribution profiles can be thought of as the probability distribution of observing a certain atom type at a given distance from the calcite walls (z-direction). It was calculated along the z-direction (perpendicular to the calcite surfaces) by tracking and time-averaging appearance of a given atom type within a set of conceptual 0.1 Å–thick bins lying parallel to the slit's axis (schematically illustrated in **Figure S7**). Distribution profiles over the slit spacing were symmetrized around the slit's axis in order to magnify important details of species distribution adjacent to the calcite surface. In all diagrams of distribution profiles, reference coordinate (z=0) is defined by the plane passing through the topmost calcium atoms of the bottom $CaCO_3$ slab. Four peaks are distinct in the distribution profile of the oxygen atom in water (O_w), as labeled in **Figure 8**. The same holds for the number density of hydrogen atom in water (Hw), shown in **Figure S8**. The number densities of O_w and H_w exhibits an oscillating profiles up to 1 nm outward from the calcite surface and eventually reach constant values characterizing a bulk-like behavior. It suggests the formation of dense wetting monolayers nearby the calcite surface. The interfacial water layering observed at spontaneous flow here is apparently similar to that reported by Koleini

et al. for case of stationary interface of the brine-calcite system [59] The primary water monolayer, labeled 1 in **Figure 8**, has been described as a solid-like layer in which water molecules are strongly held in place by strong near-surface interactions due to H-bonding with basal carbonate groups [60].

The ions structuring within the calcite-brine interface impacts their transport through the channel [33]. Sodium ions tend to accumulate adjacent to the calcite surface, as inferred by the sharp peak of the Na^+ profile at ~ 3 Å away from the substrate plane. In our previous work, it was revealed the oxygen atoms in the carbonate groups of the $CaCO_3$ basal plane are favoring binding sites for adhering Na^+ cations through inner-sphere mode[61]. Unlike sodium ions, Cl^- ions mostly appear between the third and fourth wetting layers, as seen in **Figure 8.** They accumulate in the vicinity of the calcite surface by pairing with already adsorbed Na^+ ions. [42] For the sake of completeness, density distribution profiles are compared at stabilized and early time flow (**Figure S9**). It can be seen that near-surface adsorption layers subtly evolve by water penetration inside the capillary.

There is a systematic lowering of water and ion distribution peaks with increasing brine temperature. Temperature pronouncedly effects on the distribution profile of ions to the extent that height of sodium and chloride peaks reduces appreciably upon heating the flowing brine from 300 to 360 K. It seems that water and ions are less prone to be localized near the calcite surface at higher temperatures. Not specific to this study, Giovambattista et al. explored phase behavior of water confined within hydrophilic and hydrophobic plates and pointed out weaker water structuring near walls surfaces at higher temperature [62]. Atoms become excited and move faster by gaining larger thermal (kinetic) energy at higher temperatures. As a result, they would be weakly affected by near-surface interactions.

Axial velocity profile across the channel

Velocity field within the calcite channel was obtained to further analyzing dynamics of capillary uptake and its response to temperature. **Figure 9** shows the axial water velocity profiles at Phases 1 and 3 recognized in **Figures 6-7** and different temperatures. Each profile was obtained by averaging the axial (y-component) velocity of water molecules in a set of 0.1 Å-width bins parallel to the channel walls (see **Figure S7**). The water velocity field, **Figure 9**, exhibits a plug-shape profile at the early time of capillary displacement (Phase 1). That is to say, the patches of water molecules in bins normal to the calcite walls travel together at the earliest time of water intrusion. Further, we note the finite (non-zero) water velocity close to the slit walls, indicating slippage of water molecules at the calcite walls. It should be emphasized that flow boundaries do not exactly meet bare surface of calcite walls; because the water monolayers closest to the calcite substrate are immobile, *i.e.*, with zero velocity. We also notice higher imbibition velocity by increasing brine temperature (**Figure 9**). It is consistent with faster early intrusion of water at higher temperature (**Figure 3**).

Particular to stabilized imbibition regime, the water velocity profile is parabolic-like by varying from zero close to the flow boundaries to a maximum value along the central axis of the interlayer gap. Again, the primary wetting layer adjacent to the calcite slabs remains immobile. We could argue that near-surface interactions is so strong as if the primary water monolayer sticks on the calcite surface. Similar to the early flow period, the imbibition velocity increases as a function of the brine temperature at this stage. Common in both flow regimes, the velocity profile at 330 K is closer to that of 360 K, in accordance with the displacement curves in **Figure 3**.

Discussion

It is well-documented that inserting a capillary into a wetting solution triggers its rapid suction in response to solid-liquid attractions [63]. This spontaneous process, naturally occurring in fine pores of subsurface strata, was studied here using MD simulation to gain a molecular-level insight into the dynamics of imbibing water and ion transport. To this end, 1 $mol.dm^{-3}$ NaCl solution at varying temperatures, (300, 330 and 360) K, was brought into contact with a calcite channel and its capillary uptake was analyzed during imbibition in terms of displacement length, dynamic contact angle, meniscus thickness and axial velocity field. By these considerations, water transport inside the capillary follows several consecutive flow regimes, which are discussed in the following:

Inviscid flow

At the beginning of intrusion, water advances in the channel with an almost planar meniscus up to ~1 nm. The near perpendicular contact angle at this period signifies a neutral-wet state, in conflict with the strongly hydrophilic character of neat surface of $CaCO_3$ crystals [64]. It should be noted that the chemical identity of the confining calcite slabs, and thus their wetting affinity essentially remains intact during the water adsorption. For this reason, the abnormally large meniscus angle at the very early stage of imbibition is ascribed to small contribution of capillary force relative inertia for driving the solution inside the channel. Water flows piston-likely at the earliest time of intrusion. The uniform velocity distribution perpendicular to the transport direction signifies a shear-less flow, termed *inviscid* flow [1]. Special to velocity field at this flow regime, there is a slip (non-zero) velocity adjacent to solid walls. Such slippage has frequently been pointed out for force-induced fluid transport in nano-scale pores [65].

Water intrusion is triggered by capillary suction at the pore entrance. Snapshots in **Figure S10** displays the initiation of capillary flow when meniscus edges touch corners of calcite

slabs. Water is instantly pulled into the slit and moves shortly in response to inertia (bulk momentum) effect. It is well reflected in the uniform velocity profile at this stage (**Figure 9**). Such inertia-dominated flow regime was already reported by Oyarzua et al. while studding capillary adsorption in silica nano-confinements [15]. We noticed that water displaces longer and faster during the inviscid flow regime at higher temperatures, as a result of lower density and viscosity. **Figure 10** presents density and shear viscosity of water under confinement and at different temperatures, which were obtained according to the workflow explained in sections S10-11 of SI.

Stabilized (capillary-viscous) imbibition

Following the early inviscid regime, meniscus angle, θ, drops gradually to attain an ultimate constant value. This reveals the increasing contribution of capillary force throughout water displacement within the calcite conduit, in accord with the famous Young-Laplace equation for capillary pressure, P_c [66]:

$$P_c = \frac{4\sigma \cos\theta}{H}, \quad \textbf{(1)}$$

where σ and μ stand for surface tension and viscosity of water, respectively. H denotes interlayer spacing of the slit. According to **Eq. 1** and using water properties reported in **Figure 10**, capillary pressures at stabilized flow regime are 266, 301 and 286 bar at 300, 330 and 360 K, respectively. Such extraordinary capillary pressures reflect the strong surface forces driving water within the nano-channel.

Particular to this flow regime, velocity profile across the slit aperture appears parabolic (**Figure 9**), with maximum velocity occurring along the central axis of the channel. It comes with an appreciable velocity gradient near the calcite walls, implying the significance of viscous drag. At this regime, the length displaced by water, L_t, at any instance, t, is connected

with relative magnitude of pulling capillary force and resisting viscous drag. This relationship is mathematically described by classical LW equation [67]:

$$L_t = \sqrt{H\frac{\sigma cos\theta_e}{3\mu}}\sqrt{t} \quad \textbf{(2)}$$

with subscript *e* emphasizing value of contact angle for an equilibrated (stabilized) meniscus. Since classical LW equation was developed for flow within micro-capillaries, the slit spacing, H, in **Eq. 2** should be regarded as volumetric spacing of the channel, H_V.

Penetration lengths predicted by **Eq. 2** deviate markedly from MD results, **Figure S16.a**. However, classical LW equation captures the general trend of water advance at different temperatures. In particular, the displacement curve predicted by LW theory at 330 K is closer to that of 360 K, which is consistent with atomistic results (**Figure S16.a**). Classical LW equation was developed by assuming constant meniscus angle during the capillary flow and neglecting the inertial effect [67]. Bosanquet equation is an improved version of the classical LW theory which incorporates both inertia and dynamic contact angle (detailed in section S12 of SI) [15]:

$${L_t}^2 = \frac{2A^2}{B}\left[t - \frac{1}{B}(1 - e^{-Bt})\right], \quad \textbf{(3.a)}$$

$$A = \sqrt{2\frac{\sigma \cos\theta_t}{\rho H_V}}, \quad \textbf{(3.b)}$$

$$B = \frac{12\mu}{\rho H_D^2}. \quad \textbf{(3.c)}$$

where ρ stands for mean density of liquid within the slit. H_V and H_D denotes the volumetric (total) and hydrodynamics spacing of the slit, respectively, such that $H_V > H_D$ due to diminished cross section of flow by fluid layering near solid walls. As shown in **Figure S16.b**,

the displacement lengths predicted by Bosanquet equation are fairly in agreement with MD results.

According to classical LW theory (**Eq. 2**), capillary filling rate is proportional to relative magnitude of capillary to viscous forces. In this sense, faster imbibition of hot brine (**Figure S16.a**) reveals the weaker contribution of viscous dissipation at high temperature. We already notified reduction of viscosity, surface tension (**Figure 10**) and meniscus angle (**Figure 7**) of water confined in the calcite channel upon increasing temperature. Results presented here reveal that fluid viscosity could critically impact kinetics of capillarity, depending on the fluid temperature. The central role of viscosity has been already notified in the case of two phase flow. For example, a theoretical study conducted by Wang et al. revealed that water viscosity regulates the rate of oil displacement by an aqueous solution intruding into a quartz nano-pore [20]. The decreasing trend of water contact angle with rising temperature has also been recorded in former studies. For instance, through a systematic experimental investigation on steel surfaces, Song et al. argued the stronger water wetness at elevated temperatures stems from the weakened cohesive interactions in water phase and thus, their higher tendency for adsorbing on the solid substrate [68]. It means the hot brine tends to adhere stronger on surface of the confining wall.

From a molecular viewpoint, capillary uptake is driven by progressive adsorption of water molecules on the calcite walls and forming wetting layers (**Figure 8**). The near-surface interactions are so strong that primary wetting monolayers remain immobile during the water imbibition, *i.e.*, having zero velocity (**Figure 9**). Those monolayers are even stationary at the inviscid stage of water displacement. Hence, one may hypothesize the spontaneous imbibition is ruled by diffusive spreading of molecules inside the channel. mostly at the middle of the channel. In this circumstance, water molecules in the channel center continuously move ahead and adsorb on the calcite walls to form wetting layers. MSD diagrams (**Figure 5)** highlight the increasing role of water diffusion beyond the early inviscid flow regime.

End effect

Dynamic features of a fluid leaving a nano-capillary has been vastly neglected in former researches. Our analyses revealed the special behavior of solution upon leaving the calcite slit. In this process, water displacement curve does not comply with classical LW relationship and water frontier passes the channel outlet at a constant pace of advancement. Judging by snapshots captured at the end of imbibition process, the leading contact lines of the meniscus spread towards the exterior edges of calcite slabs. As shown in **Figure S18**, the velocity field at this stage appears parabolic, similar to the velocity profile of stabilized flow regime (**Figure 9**). It implies the viscous dissipation appreciably contributes to the meniscus movement at the channel outlet, even though the displacement profiles varies linearly at this stage (**Figure 3)**. Throughout, we expect stronger near-surface interactions as a result of the brine phase excessively touching the calcite surface. This is well mirrored into the meniscus angle dropped to zero at late stage of imbibition (**Figure 7**). One could think of the special balance of viscous and near-surface forces causing the peculiar dynamics of water displacement at the slit outlet. Moving forward, we will further scrutinize this special imbibition regime.

Ion transfer in the calcite channel

It was recognized the hydrodynamics of water phase impacts transport of sodium and chloride ions throughout all flow regimes described above. Even, ions localization at the calcite interface is connected with axial travelling of water molecules. We know from former investigations that sodium cations tend to adhere directly on the calcite surface through pairing with protruding oxygen atoms of basal carbonate groups; thus, forming a positively-charged layer over the calcite surface [53,69]. It is mirrored into the sharp peak of Na^+ distribution profile, shown in **Figure 8**. In comparison to the static contact of NaCl brine-calcite [38,61], two

extra peaks emerge in the distribution profile of Na^+ cation in case of water imbibition into the calcite slit (**Figure 11**). The primary peak of Na^+ diminishes at dynamic condition as well. We further notice that 1st and 2nd maxima of O_w and H_w distribution profiles are markedly larger at dynamic (imbibition) condition compared to static state (**Figure 11**). It implies the greater ability of water molecules to occupy interstitial sites on calcite surface when imbibing into an empty capillary. It can be argued that denser wetting layers formed by imbibing solution inhibit direct access of Na^+ ions to the calcite surface. Upon this argument, the extra peaks appeared in the distribution profile of Na^+ cations could be ascribed to ions entrained by water molecules at moving wetting layers. For chloride, three peaks are distinguished in **Figure 11**, with the primary one lacking at dynamic condition. Apparently, water imbibition does not appreciably impact distribution of Cl^- anions at calcite interface in this work.

In sum, Ions transfer within the calcite slit in response to their own thermal (kinetics) energy, interaction with the confining calcite slabs, and hydrodynamics and diffusion of solvating water phase. Therefore, slit geometry (particularly, interlayer spacing) and salt concentration would play a determining role on the behavior of ions inside the capillary. Future works will examine impact of those parameters on capillary flow of saline solutions under nano-confinement.

Conclusions

This research concerned spontaneous uptake of a NaCl solution by a calcite nano-capillary. By employing atomistic simulation, dynamics and surface structuring of ions and water molecules were assess throughout the imbibition process at a wide range of temperature. Depending on the relative contribution of surface (capillary) force, viscous drag and inertia, solution experiences distinct, consecutive capillarity regimes within the nano-channel. Displacement is triggered by capillary suction and then, solution advances piston-likely, *i.e.*, with uniform velocity profile and a near planar interface, in response to inertia effect. Following

this so-called inviscid (or early time) flow regime, imbibition transients to stabilized capillary-viscous displacement, where meniscus angle falls to a stabilized value. Meanwhile, brine advances diffusively by progressive adsorption of water molecules on walls of confining calcite slabs to form wetting monolayers. Eventually, a peculiar imbibing regime emerges by approaching to the channel outlet, in which water moves at constant velocity as a result of contact lines touching corners and exterior edges of solid slabs. Throughout the capillary filling, Na^+ and Cl^- ions transport synchronously inside the calcite slit with their motion tightly coupled to hydrodynamic and diffusion of water. We observed disparate distribution of ions and water molecules adjacent to calcite walls at static and imbibing states.

Brine transports faster within the channel by increasing temperature and should travel longer in the slit to develop a stabilized meniscus, *i.e.*, with constant contact angle and interface thickness. Density, surface tension, viscosity and equilibrium contact angle reduces by elevating temperature of confined solution. Also, ions and water weakly localize nearby the calcite surface at high temperature. By comparing displacement diagrams obtained by MD simulation and classical Lucas-Washburn equation, the faster capillary flow of water at higher temperature was ascribed to diminished contribution of viscous friction relative to capillary attraction.

ASSOCIATED CONTENT

Supporting Information

The Supporting Information is available free of charge on the ACS Publications website at DOI:

Verifying insolubility of calcite slabs during water imbibition; workflows for tracking meniscus angle and water frontier; Displacement curves of ions (sodium: closed circles and chloride: open squares), meniscus leading margins (red solid curve) and bottom arcs; Comparing density distribution profiles of O_w, H_w, Na^+ and Cl^- obtained as stabilized and early time flow; Methodology for calculating density and viscosity of water under confinement; MSD of water at different temperatures; Deriving Bosanquet and Lucas-Washburn equations and comparing their predictions.

AUTHOR INFORMATION

Corresponding Author

***Email:** shahab@sharif.edu & dr.ayatollahi@gmail.com

ORCID

Mohammad Hasan Badizad: 0000-0001-8144-6896

Mohammad Mehdi Koleini: 0000-0001-7950-951X

Hugh Christopher Greenwell: 0000-0001-5719-8415

Shahab Ayatollahi: 0000-0001-7561-6393

Mohammad Hossein Ghazanfari: 0000-0001-7512-8728

Notes

The authors declare no competing financial interest.

References

(1) Lim, H.; Tripathi, A.; Lee, J. Dynamics of a Capillary Invasion in a Closed-End Capillary. *Langmuir* **2014**, *30* (31), 9390–9396. https://doi.org/10.1021/la501927c.

(2) Piroird, K.; Clanet, C.; Que□re□, D. Capillary Extraction. *Langmuir* **2011**, *27* (15), 9396–9402. https://doi.org/10.1021/la201490m.

(3) Hasan Badizad, M.; Mehdi Koleini, M.; Hartkamp, R.; Ayatollahi, S.; Hossein Ghazanfari, M. How Do Ions Contribute to Brine-Hydrophobic Hydrocarbon Interfaces? An In Silico Study. *J. Colloid Interface Sci.* **2020**. https://doi.org/10.1016/j.jcis.2020.04.060.

(4) Koleini, M. M.; Badizad, M. H.; Ghatee, M. H.; Ayatollahi, S. An Atomistic Insight into the Implications of Ion-Tuned Water Injection in Wetting Preferences of Carbonate Reservoirs. *J. Mol. Liq.* **2019**. https://doi.org/10.1016/j.molliq.2019.111530.

(5) Bradley, P. M.; Journey, C. A.; Chapelle, F. H.; Lowery, M. A.; Conrads, P. A. Flood Hydrology and Methylmercury Availability in Coastal Plain Rivers. *Environ. Sci. Technol.* **2010**, *44* (24), 9285–9290. https://doi.org/10.1021/es102917j.

(6) Erfani, H.; Joekar-Niasar, V.; Farajzadeh, R. Impact of Microheterogeneity on Upscaling Reactive Transport in Geothermal Energy. *ACS Earth Sp. Chem.* **2019**, *3* (9), 2045–2057. https://doi.org/10.1021/acsearthspacechem.9b00056.

(7) Knaus, E.; Killen, J.; Biglarbigi, K.; Crawford, P. An Overview of Oil Shale Resources. In *ACS Symposium Series*; 2010; pp 3–20. https://doi.org/10.1021/bk-2010-1032.ch001.

(8) Yan, H.; Yuan, S. Molecular Dynamics Simulation of the Oil Detachment Process within Silica Nanopores. *J. Phys. Chem. C* **2016**, *120* (5), 2667–2674. https://doi.org/10.1021/acs.jpcc.5b09841.

(9) Shirono, K.; Daiguji, H. Molecular Simulation of the Phase Behavior of Water Confined in Silica Nanopores. *J. Phys. Chem. C* **2007**, *111* (22), 7938–7946. https://doi.org/10.1021/jp067380g.

(10) Dai, H.; Xu, Z.; Yang, X. Water Permeation and Ion Rejection in Layer-by-Layer Stacked Graphene Oxide Nanochannels: A Molecular Dynamics Simulation. *J. Phys. Chem. C* **2016**, *120* (39), 22585–22596. https://doi.org/10.1021/acs.jpcc.6b05337.

(11) Enyashin, A. N.; Kreizman, R.; Seifert, G. Capillary Imbibition of PbI 2 Melt by Inorganic and Carbon Nanotubes. *J. Phys. Chem. C* **2009**, *113* (31), 13664–13669. https://doi.org/10.1021/jp903649w.

(12) Ganjiani, S. H.; Hossein Nezhad, A. Molecular Dynamics Simulation of the Effects of the Carbon–Water Interaction Parameters on the Nanofluidic Energy Absorption System. *J. Phys. Chem. C* **2016**, *120* (22), 11864–11870. https://doi.org/10.1021/acs.jpcc.6b00421.

(13) Liu, L.; Bhatia, S. K. Molecular Simulation of CO 2 Adsorption in the Presence of Water in Single-Walled Carbon Nanotubes. *J. Phys. Chem. C* **2013**, *117* (26), 13479–13491. https://doi.org/10.1021/jp403477y.

(14) Zambrano, H. A.; Walther, J. H.; Jaffe, R. L. Molecular Dynamics Simulations of Water on a Hydrophilic Silica Surface at High Air Pressures. *J. Mol. Liq.* **2014**, *198*, 107–113. https://doi.org/10.1016/j.molliq.2014.06.003.

(15) Oyarzua, E.; Walther, J. H.; Mejía, A.; Zambrano, H. A. Early Regimes of Water Capillary Flow in Slit Silica Nanochannels. *Phys. Chem. Chem. Phys.* **2015**, *17* (22), 14731–14739. https://doi.org/10.1039/C5CP01862E.

(16) Karna, N. K.; Oyarzua, E.; Walther, J. H.; Zambrano, H. A. Effect of the Meniscus Contact Angle during Early Regimes of Spontaneous Imbibition in Nanochannels. *Phys. Chem. Chem. Phys.* **2016**, *18* (47), 31997–32001. https://doi.org/10.1039/C6CP06155A.

(17) Prakash, S.; Zambrano, H. A.; Fuest, M.; Boone, C.; Rosenthal-Kim, E.; Vasquez, N.; Conlisk, A. T. Electrokinetic Transport in Silica Nanochannels with Asymmetric Surface Charge. *Microfluid. Nanofluidics* **2015**, *19* (6), 1455–1464. https://doi.org/10.1007/s10404-015-1659-0.

(18) Hou, D.; Jia, Y.; Yu, J.; Wang, P.; Liu, Q. Transport Properties of Sulfate and Chloride Ions Confined between Calcium Silicate Hydrate Surfaces: A Molecular Dynamics Study. *J. Phys. Chem. C* **2018**, *122* (49), 28021–28032. https://doi.org/10.1021/acs.jpcc.8b07484.

(19) Wang, P.; Zhang, Q.; Wang, M.; Yin, B.; Hou, D.; Zhang, Y. Atomistic Insights into Cesium Chloride Solution Transport through the Ultra-Confined Calcium–Silicate–Hydrate Channel. *Phys. Chem. Chem. Phys.* **2019**, *21* (22), 11892–11902. https://doi.org/10.1039/C8CP07676F.

(20) Wang, X.; Xiao, S.; Zhang, Z.; He, J. Displacement of Nanofluids in Silica Nanopores: Influenced by Wettability of Nanoparticles and Oil Components. *Environ. Sci. Nano* **2018**, *5* (11), 2641–2650. https://doi.org/10.1039/C8EN00704G.

(21) Wang, X.; Zhang, Z.; Torsæter, O.; He, J. Atomistic Insights into the Nanofluid Transport through an Ultra-Confined Capillary. *Phys. Chem. Chem. Phys.* **2018**, *20* (7), 4831–4839. https://doi.org/10.1039/C7CP08140E.

(22) Wang, X.; Xiao, S.; Zhang, Z.; He, J. Transportation of Janus Nanoparticles in Confined Nanochannels: A Molecular Dynamics Simulation. *Environ. Sci. Nano* **2019**, *6* (9), 2810–2819. https://doi.org/10.1039/C9EN00314B.

(23) Sedghi, M.; Piri, M.; Goual, L. Atomistic Molecular Dynamics Simulations of Crude Oil/Brine Displacement in Calcite Mesopores. *Langmuir* **2016**, *32* (14), 3375–3384.

(24) Brian Jones, C. F. K. Dendritic Calcite Crystals Formed by Calcification of Algal Filaments in a Vadose Environment. *SEPM J. Sediment. Res.* **1986**, *Vol. 56*. https://doi.org/10.1306/212F88C3-2B24-11D7-8648000102C1865D.

(25) Monchau, F.; Hivart, P.; Genestie, B.; Chai, F.; Descamps, M.; Hildebrand, H. F. Calcite as a Bone Substitute. Comparison with Hydroxyapatite and Tricalcium Phosphate with Regard to the Osteoblastic Activity. *Mater. Sci. Eng. C* **2013**, *33* (1), 490–498. https://doi.org/10.1016/j.msec.2012.09.019.

(26) Constantz, B. R. Coral Skeleton Construction: A Physiochemically Dominated Process. *Palaios* **1986**, *1* (2), 152. https://doi.org/10.2307/3514508.

(27) KESTER, D. R.; DUEDALL, I. W.; CONNORS, D. N.; PYTKOWICZ, R. M. PREPARATION OF ARTIFICIAL SEAWATER. *Limnology and Oceanography*. 1967. https://doi.org/10.4319/lo.1967.12.1.0176.

(28) Sedghi, M.; Piri, M.; Goual, L. Atomistic Molecular Dynamics Simulations of Crude Oil/Brine Displacement in Calcite Mesopores. *Langmuir* **2016**, *32* (14), 3375–3384. https://doi.org/10.1021/acs.langmuir.5b04713.

(29) Santos, M. S.; Franco, L. F. M.; Castier, M.; Economou, I. G. Molecular Dynamics Simulation of n -Alkanes and CO 2 Confined by Calcite Nanopores. *Energy & Fuels* **2018**, *32* (2), 1934–1941. https://doi.org/10.1021/acs.energyfuels.7b02451.

(30) Lord, H. L.; Zhan, W.; Pawliszyn, J. Fundamentals and Applications of Needle Trap Devices. *Anal. Chim. Acta* **2010**, *677* (1), 3–18. https://doi.org/10.1016/j.aca.2010.06.020.

(31) Ghatee, M. H.; Koleini, M. M.; Ayatollahi, S. Molecular Dynamics Simulation Investigation of Hexanoic Acid Adsorption onto Calcite (<mml:Math Altimg="si4.Gif" Overflow="scroll" Xmlns:Xocs="http://Www.Elsevier.Com/Xml/Xocs/Dtd" Xmlns:Xs="http://Www.W3.Org/2001/XMLSchema" Xmlns:Xsi="http://Www.W3.Org/2. *Fluid Phase Equilib.* **2015**, *387*, 24–31. https://doi.org/10.1016/j.fluid.2014.11.029.

(32) Martínez, L.; Andrade, R.; Birgin, E. G.; Martínez, J. M. PACKMOL: A Package for Building Initial Configurations for Molecular Dynamics Simulations. *J. Comput. Chem.* **2009**, *30* (13), 2157–2164. https://doi.org/10.1002/jcc.21224.

(33) Dongshuai, H.; Zeyu, L.; Peng, Z.; Qingjun, D. Molecular Structure and Dynamics of an Aqueous Sodium Chloride Solution in Nano-Pores between Portlandite Surfaces: A Molecular Dynamics Study. *Phys. Chem. Chem. Phys.* **2016**, *18* (3), 2059–2069. https://doi.org/10.1039/c5cp05884h.

(34) Plimpton, S.; Crozier, P.; Thompson, A. LAMMPS-Large-Scale Atomic/Molecular Massively Parallel Simulator. *Sandia Natl. Lab.* **2007**.

(35) Xiao, S.; Edwards, S. A.; Gräter, F. A New Transferable Forcefield for Simulating the Mechanics of CaCO 3 Crystals. *J. Phys. Chem. C* **2011**, *115* (41), 20067–20075. https://doi.org/10.1021/jp202743v.

(36) Jorgensen, W. L.; Chandrasekhar, J.; Madura, J. D.; Impey, R. W.; Klein, M. L. Comparison of Simple Potential Functions for Simulating Liquid Water. *J. Chem. Phys.* **1983**, *79* (2), 926–935. https://doi.org/10.1063/1.445869.

(37) Joung, I. S.; Cheatham, T. E. Determination of Alkali and Halide Monovalent Ion Parameters for Use in Explicitly Solvated Biomolecular Simulations. *J. Phys. Chem. B* **2008**, *112* (30), 9020–9041. https://doi.org/10.1021/jp8001614.

(38) Koleini, M. M.; Badizad, M. H.; Ayatollahi, S. An Atomistic Insight into Interfacial Properties of Brine Nanofilm Confined between Calcite Substrate and Hydrocarbon Layer. *Appl. Surf. Sci.* **2019**, *490*, 89–101. https://doi.org/10.1016/j.apsusc.2019.05.337.

(39) Ellis, A. J. The Solubility of Calcite in Sodium Chloride Solutions at High Temperatures. *Am. J. Sci.* **1963**, *261* (3), 259–267. https://doi.org/10.2475/ajs.261.3.259.

(40) Millero, F. J.; Milne, P. J.; Thurmond, V. L. The Solubility of Calcite, Strontianite and Witherite in NaCl Solutions at 25°C. *Geochim. Cosmochim. Acta* **1984**, *48* (5), 1141–1143. https://doi.org/10.1016/0016-7037(84)90205-9.

(41) Pokrovsky, O. S.; Golubev, S. V.; Schott, J. Dissolution Kinetics of Calcite, Dolomite and Magnesite at 25 °C and 0 to 50 Atm PCO2. *Chem. Geol.* **2005**, *217* (3–4), 239–255. https://doi.org/10.1016/j.chemgeo.2004.12.012.

(42) Ricci, M.; Spijker, P.; Stellacci, F.; Molinari, J.-F.; Voïtchovsky, K. Direct Visualization of Single Ions in the Stern Layer of Calcite. *Langmuir* **2013**, *29* (7), 2207–2216. https://doi.org/10.1021/la3044736.

(43) BĚHRÁDEK, J. TEMPERATURE COEFFICIENTS IN BIOLOGY. *Biol. Rev.* **1930**, *5* (1), 30–58. https://doi.org/10.1111/j.1469-185X.1930.tb00892.x.

(44) Deming, D. Application of Bottom-Hole Temperature Corrections in Geothermal

Studies. *Geothermics* **1989**, *18* (5–6), 775–786. https://doi.org/10.1016/0375-6505(89)90106-5.

(45) Nowak, T. J. The Estimation of Water Injection Profiles From Temperature Surveys. *J. Pet. Technol.* **1953**, *5* (08), 203–212. https://doi.org/10.2118/953203-G.

(46) Dimitrov, D. I.; Milchev, A.; Binder, K. Capillary Rise in Nanopores: Molecular Dynamics Evidence for the Lucas-Washburn Equation. *Phys. Rev. Lett.* **2007**, *99* (5), 054501. https://doi.org/10.1103/PhysRevLett.99.054501.

(47) Butt, H.; Graf, K.; Kappl, M. *Physics and Chemistry of Interfaces*; Wiley, 2003. https://doi.org/10.1002/3527602313.

(48) Martic, G.; Gentner, F.; Seveno, D.; Coulon, D.; De Coninck, J.; Blake, T. D. A Molecular Dynamics Simulation of Capillary Imbibition. *Langmuir* **2002**, *18* (21), 7971–7976. https://doi.org/10.1021/la020068n.

(49) Stroberg, W.; Keten, S.; Liu, W. K. Hydrodynamics of Capillary Imbibition under Nanoconfinement. *Langmuir* **2012**, *28* (40), 14488–14495. https://doi.org/10.1021/la302292w.

(50) Mills; Lobo. *Self-Diffusion in Electrolyte Solutions: A Critical Examination of Data Compiled from the Literature*; 2013.

(51) Sparkman, O. D.; Penton, Z.; Kitson, F. G. *Gas Chromatography and Mass Spectrometry*; Elsevier, 2011. https://doi.org/10.1016/C2009-0-17039-3.

(52) Koleini, M. M.; Mehraban, M. F.; Ayatollahi, S. Effects of Low Salinity Water on Calcite/Brine Interface: A Molecular Dynamics Simulation Study. *Colloids Surfaces A Physicochem. Eng. Asp.* **2018**, *537*, 61–68.

(53) Koleini, M. M.; Badizad, M. H.; Hartkamp, R.; Ayatollahi, S.; Ghazanfari, M. H. The Impact of Salinity on the Interfacial Structuring of an Aromatic Acid at the Calcite/Brine Interface: An Atomistic View on Low Salinity Effect. *J. Phys. Chem. B* **2020**, *124* (1), 224–233. https://doi.org/10.1021/acs.jpcb.9b06987.

(54) Koleini, M. M.; Badizad, M. H.; Kargozarfard, Z.; Ayatollahi, S. Interactions between Rock/Brine and Oil/Brine Interfaces within Thin Brine Film Wetting Carbonates: A Molecular Dynamics Simulation Study. *Energy & Fuels* **2019**, *33* (9), 7983–7992. https://doi.org/10.1021/acs.energyfuels.9b00496.

(55) Michalet, X. Mean Square Displacement Analysis of Single-Particle Trajectories with Localization Error: Brownian Motion in an Isotropic Medium. *Phys. Rev. E* **2010**, *82* (4), 041914. https://doi.org/10.1103/PhysRevE.82.041914.

(56) Zhao, J.; Yao, G.; Ramisetti, S. B.; Hammond, R. B.; Wen, D. Molecular Dynamics

Simulation of the Salinity Effect on the n -Decane/Water/Vapor Interfacial Equilibrium. *Energy & Fuels* **2018**, *32* (11), 11080–11092. https://doi.org/10.1021/acs.energyfuels.8b00706.

(57) Wu, J.; He, J.; Torsater, O.; Zhang, Z. Effect of Nanoparticles on Oil-Water Flow in a Confined Nanochannel: A Molecular Dynamics Study. In *SPE International Oilfield Nanotechnology Conference and Exhibition*; Society of Petroleum Engineers, 2012. https://doi.org/10.2118/156995-MS.

(58) Keller, K. S.; Olsson, M. H. M.; Yang, M.; Stipp, S. L. S. Adsorption of Ethanol and Water on Calcite: Dependence on Surface Geometry and Effect on Surface Behavior. *Langmuir* **2015**, *31* (13), 3847–3853. https://doi.org/10.1021/la504319z.

(59) Fenter, P.; Kerisit, S.; Raiteri, P.; Gale, J. D. Is the Calcite-Water Interface Understood? Direct Comparisons of Molecular Dynamics Simulations with Specular X-Ray Reflectivity Data. *J. Phys. Chem. C* **2013**, *117* (10), 5028–5042. https://doi.org/10.1021/jp310943s.

(60) Lardge, J. S.; Duffy, D. M.; Gillan, M. J. Investigation of the Interaction of Water with the Calcite (10.4) Surface Using Ab Initio Simulation. *J. Phys. Chem. C* **2009**, *113* (17), 7207–7212. https://doi.org/10.1021/jp806109y.

(61) Koleini, M. M.; Badizad, M. H.; Kargozarfard, Z.; Ayatollahi, S. The Impact of Salinity on Ionic Characteristics of Thin Brine Film Wetting Carbonate Minerals: An Atomistic Insight. *Colloids Surfaces A Physicochem. Eng. Asp.* **2019**, *571*, 27–35. https://doi.org/10.1016/j.colsurfa.2019.03.070.

(62) Giovambattista, N.; Rossky, P. J.; Debenedetti, P. G. Effect of Temperature on the Structure and Phase Behavior of Water Confined by Hydrophobic, Hydrophilic, and Heterogeneous Surfaces †. *J. Phys. Chem. B* **2009**, *113* (42), 13723–13734. https://doi.org/10.1021/jp9018266.

(63) Joly, L. Capillary Filling with Giant Liquid/Solid Slip: Dynamics of Water Uptake by Carbon Nanotubes. *J. Chem. Phys.* **2011**, *135* (21), 214705. https://doi.org/10.1063/1.3664622.

(64) Zeng, H.; Zou, F.; Horvath-Szabo, G.; Andersen, S. Effects of Brine Composition on the Adsorption of Benzoic Acid on Calcium Carbonate. *Energy & Fuels* **2012**, *26* (7), 4321–4327. https://doi.org/10.1021/ef300165m.

(65) Li, Y.; Xu, J.; Li, D. Molecular Dynamics Simulation of Nanoscale Liquid Flows. *Microfluid. Nanofluidics* **2010**, *9* (6), 1011–1031. https://doi.org/10.1007/s10404-010-0612-5.

(66) Yeung, A.; Dabros, T.; Masliyah, J. Dissipative Interfaces and Departures from the

Young−Laplace Equation. *Langmuir* **1997**, *13* (24), 6597–6606. https://doi.org/10.1021/la9706835.

(67) Hamraoui, A.; Nylander, T. Analytical Approach for the Lucas–Washburn Equation. *J. Colloid Interface Sci.* **2002**, *250* (2), 415–421. https://doi.org/10.1006/jcis.2002.8288.

(68) Song, J.-W.; Zeng, D.-L.; Fan, L.-W. Temperature Dependence of Contact Angles of Water on a Stainless Steel Surface at Elevated Temperatures and Pressures: In Situ Characterization and Thermodynamic Analysis. *J. Colloid Interface Sci.* **2020**, *561*, 870–880. https://doi.org/10.1016/j.jcis.2019.11.070.

(69) Chen, H.; Panagiotopoulos, A. Z.; Giannelis, E. P. Atomistic Molecular Dynamics Simulations of Carbohydrate-Calcite Interactions in Concentrated Brine. *Langmuir* **2015**, *31* (8), 2407–2413. https://doi.org/10.1021/la504595g.

Figures

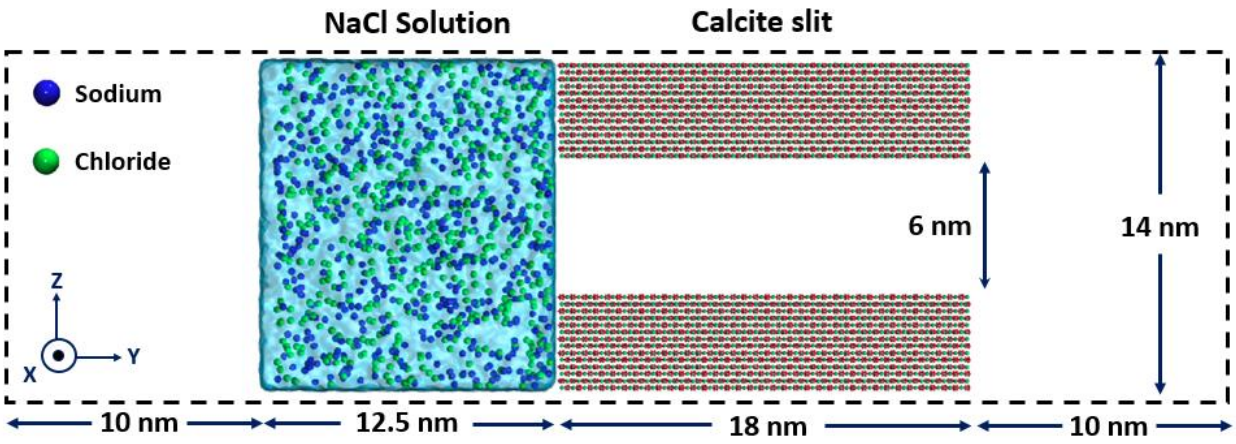

Figure 1 Initial configuration of the atomistic model of 1 mol.dm^{-3} NaCl solution imbibing into a $CaCO_3$ nano-channel.

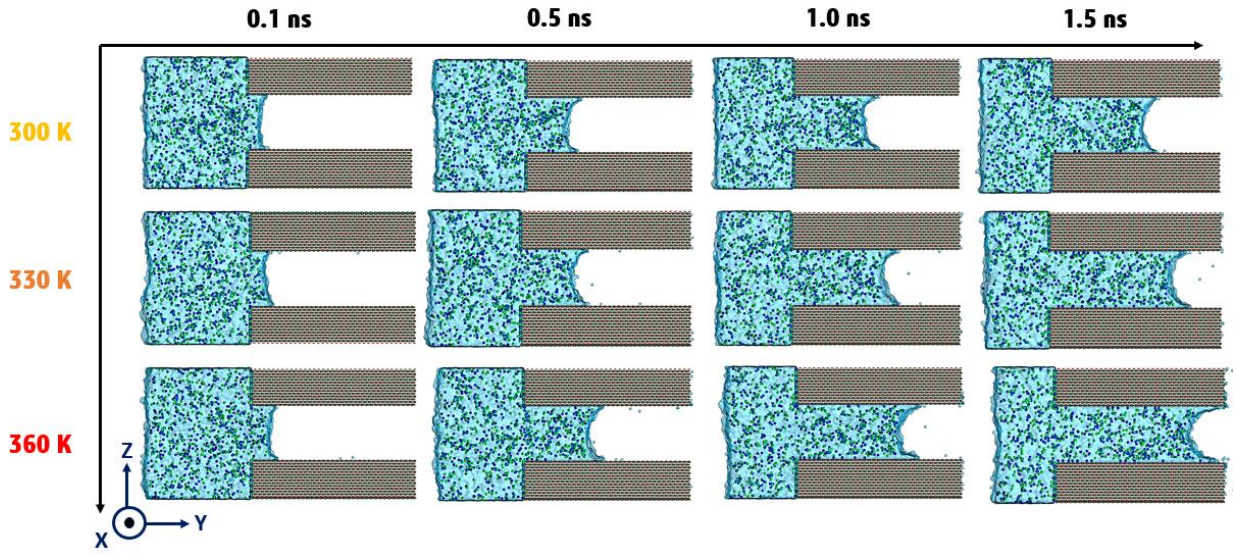

Figure 2 Snapshots of brine imbibition in the calcite slit taken at certain instances: (0.1, 0.5, 1.0 and 1.5) ns, at different temperatures (300, 330 and 360) K. Note the channel's axis is aligned with Y-axis.

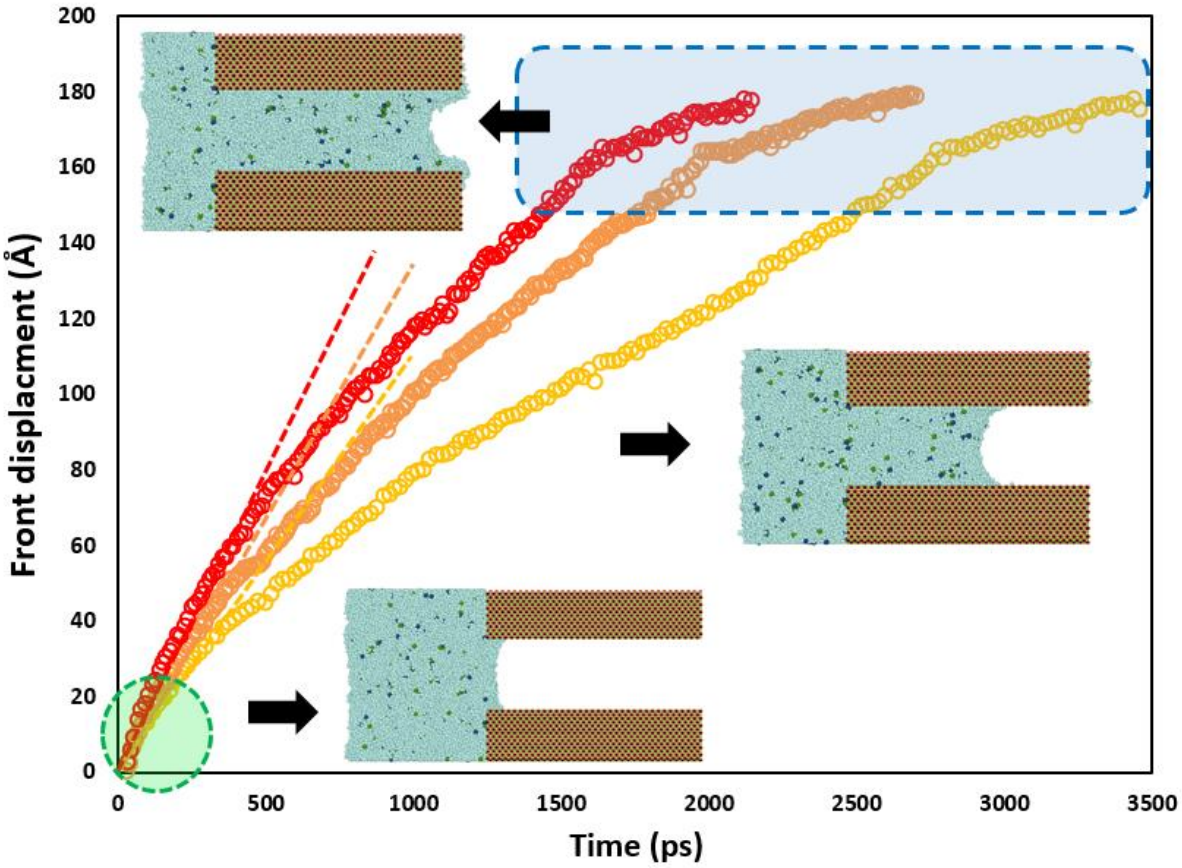

Figure 3 Penetration length (open circles) of water in the calcite capillary as a function of time at different temperatures (300K: yellow, 330K: orange, and 360K: red). Two constant velocity regimes are distinguished at very beginning and late stage of brine displacement, identified by green circle and blue rectangle, respectively.

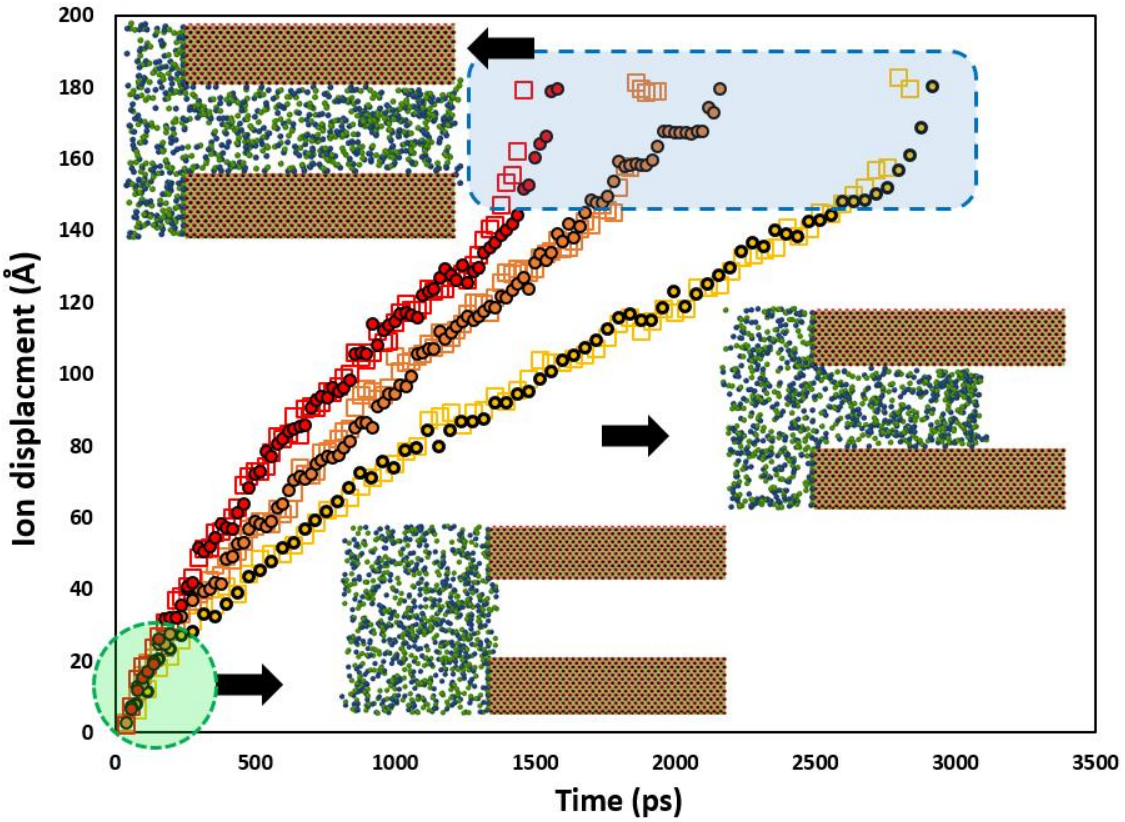

Figure 4 Temporal evolution of Na^{+} (open squares) and Cl^{-} (filled circles) ions transport within the calcite channel at different temperatures (300K: yellow, 330K: orange, and 360K: red). The early and late stages of brine penetration is identified by green circle and blue rectangle, respectively.

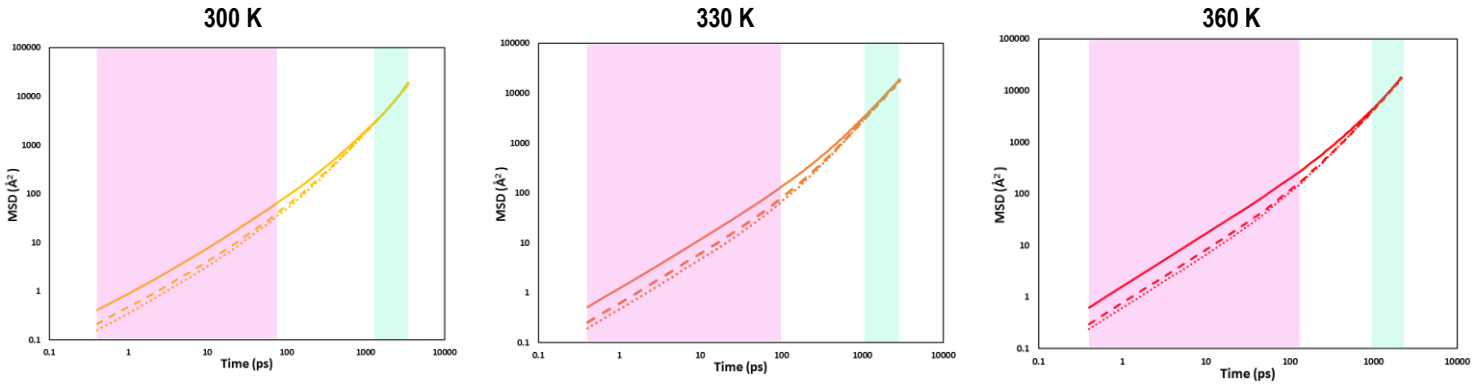

Figure 5 MSD diagrams of water (solid line), Na^+ (dashed line) and Cl^- (dotted line) at different temperatures (300K: yellow, 330K: orange, and 360K: red). Two diffusion regimes are highlighted in purple and blue.

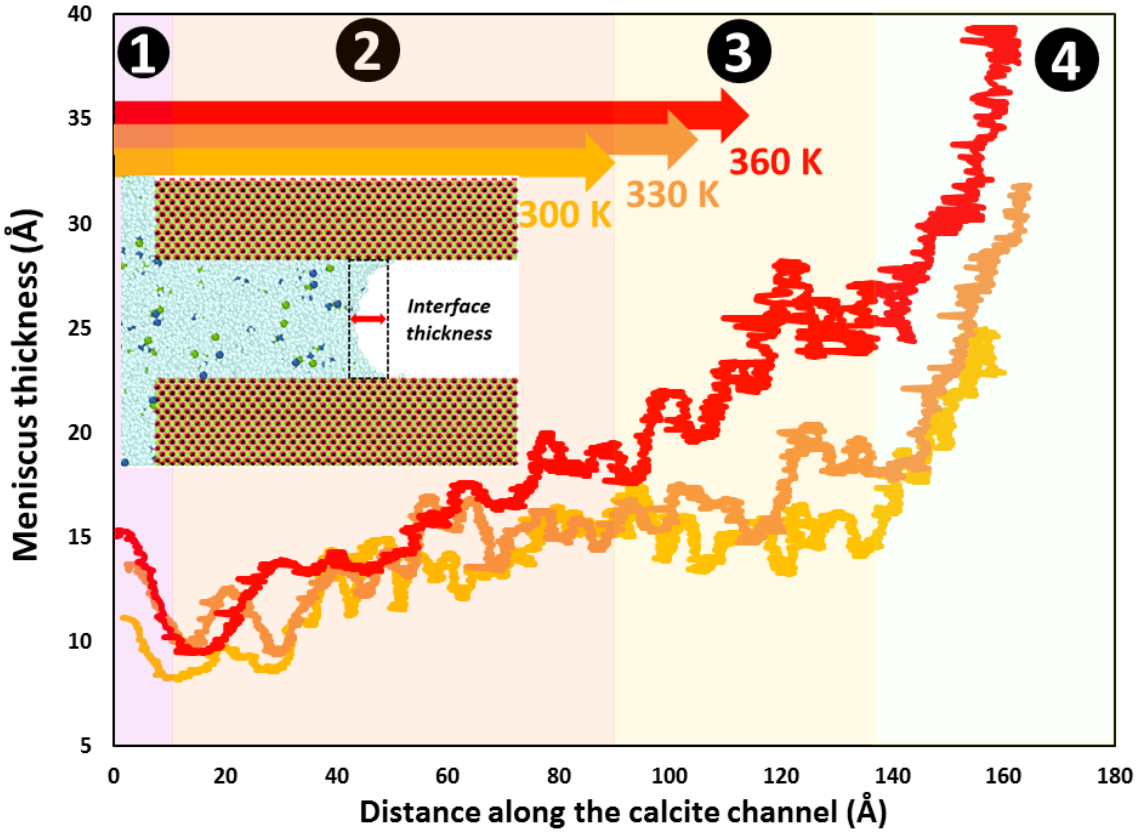

Figure 6 Meniscus thickness varies with respect to location of brine frontier in calcite slit at different temperatures (300K: yellow, 330K: orange, and 360K: red). Meniscus thickness is defined schematically in the inset.

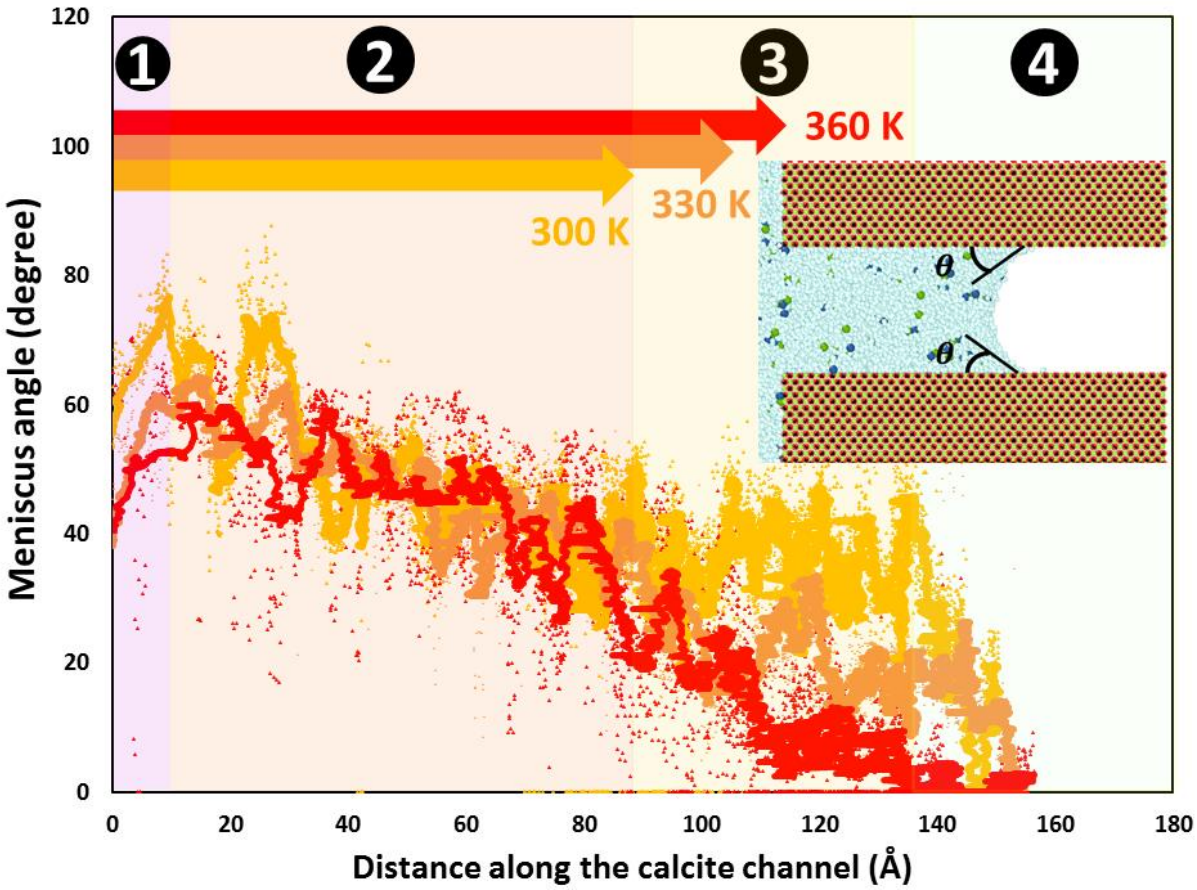

Figure 7 Dynamic contact angle at varying positions of water frontier in the calcite slit shown for different temperatures (300K: yellow, 330K: orange, and 360K: red). The arrows specify the end of meniscus developing stage at corresponding temperatures. The MD results are shown as scatter points and solid lines are corresponding running averages. Meniscus angle is defined schematically in the inset.

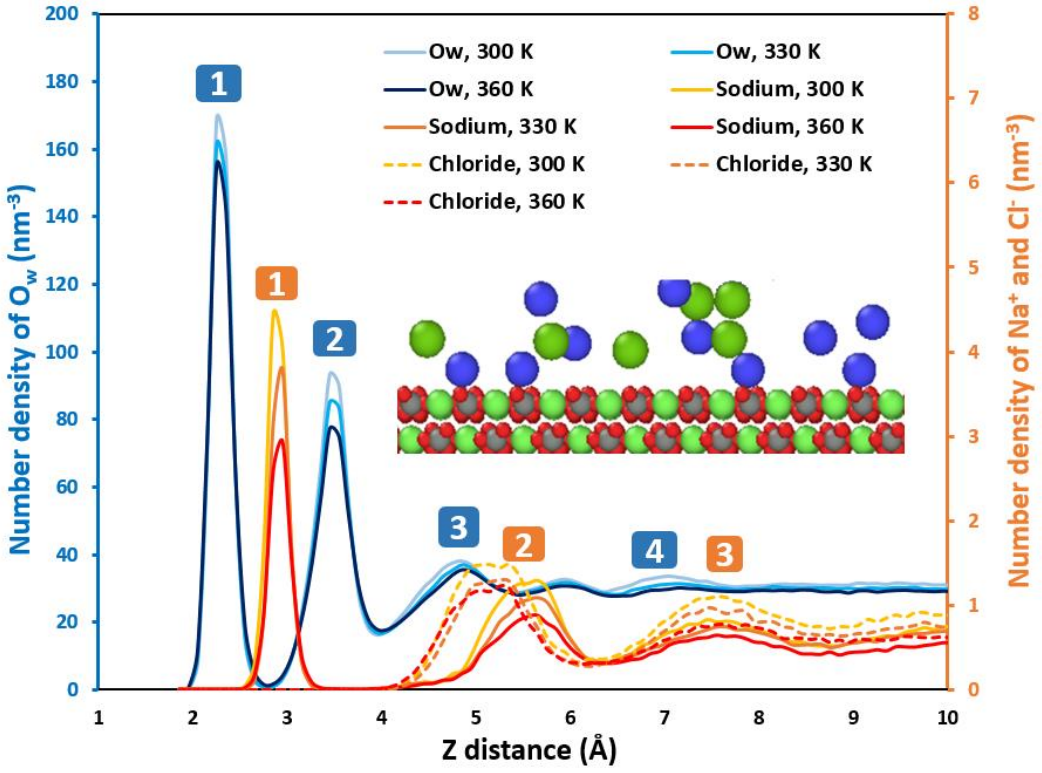

Figure 8 Density distribution profiles of oxygen atoms in water (O_w), Na^+ and Cl^- ions adjacent to the calcite surface. The reference coordinate (z=0) corresponds to the plane passing the outmost calcium ions of the calcite substrate. Peaks in each diagram are labeled consecutively. The color codes for atoms shown in the inset are sodium: blue, chloride: dark green, calcium: light green, carbon: black, and oxygen: red.

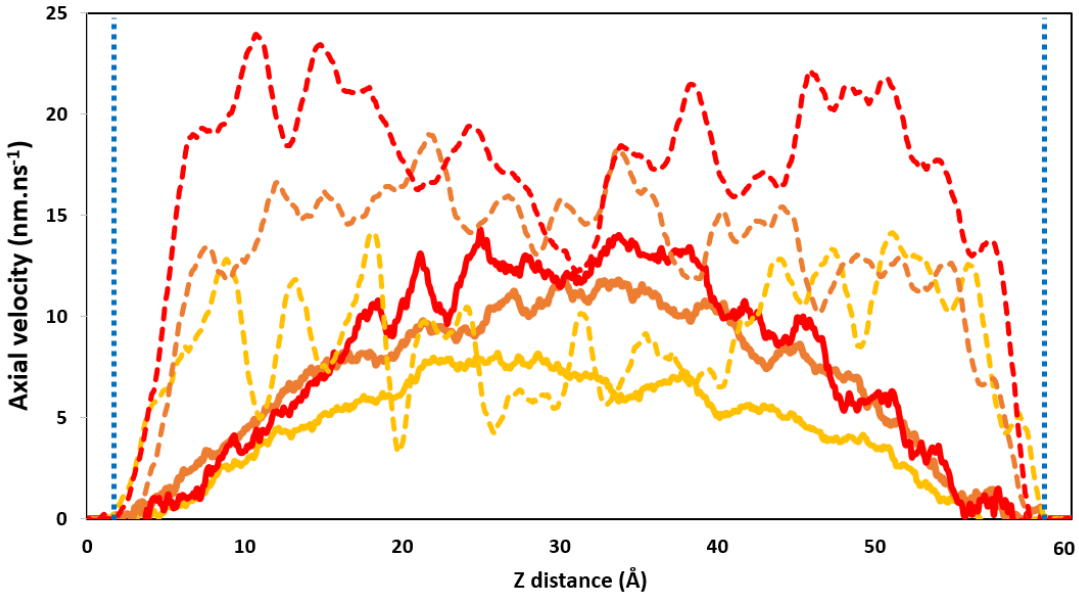

Figure 9 Axial velocity profile of water in the calcite slit obtained at Phase 1 (dotted lines) and Phase 3 (solid lines). The dotted vertical lines indicate positions of primary wetting layers, *i.e.*, primary peaks in O_w density profiles.

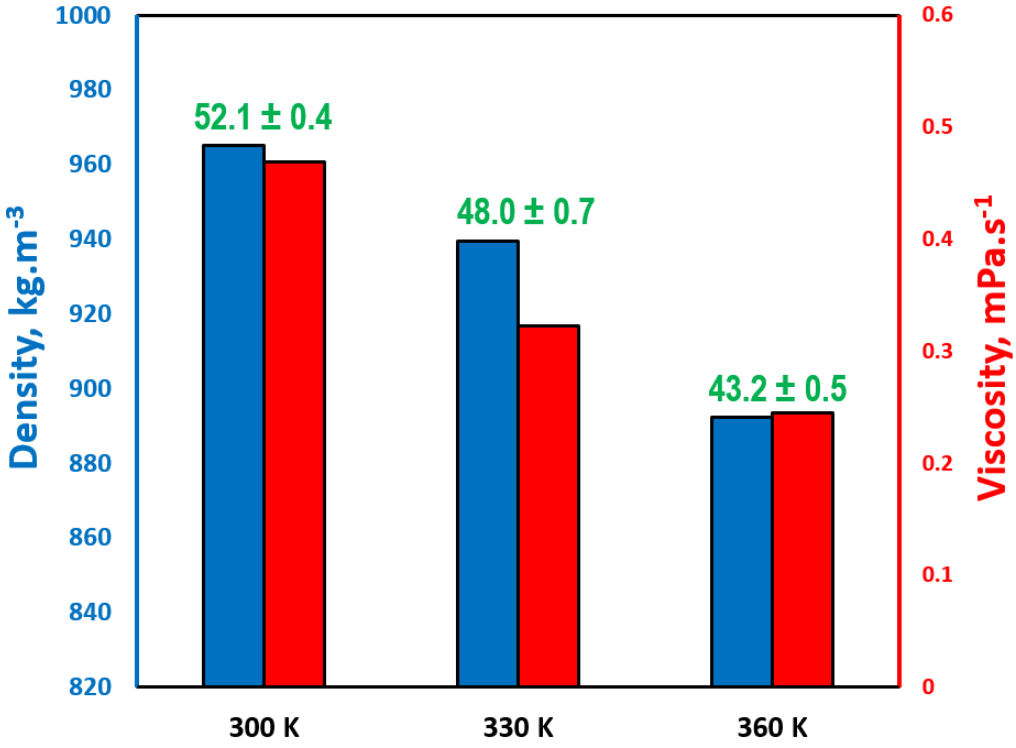

Figure 10 Density (blue bars), viscosity (red bars) and surface tension (above each bar, in units of $mN.m^{-1}$) of TIP3P water confined within a calcite slit of 6nm spacing at different temperatures.

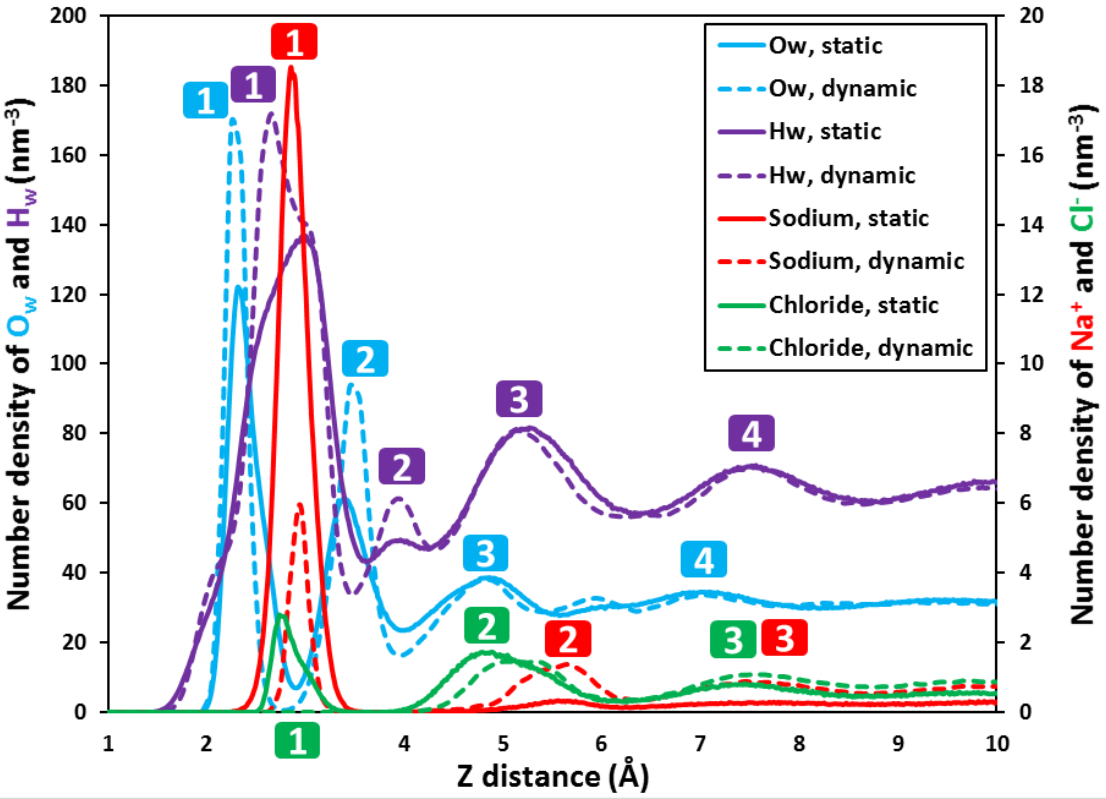

Figure 11 Density distribution profiles of oxygen atoms in water (O_w), hydrogen atoms in water (H_w), Na^+ and Cl^- ions adjacent to the calcite surface obtained at dynamic (imbibing flow) and static states using data adopted from Koleini et al. [53]. The reference coordinate (z=0) corresponds to the plane passing the outmost calcium ions of the calcite substrate. Peaks in each diagram are labeled consecutively. The color codes for atoms shown in the inset are sodium: blue, chloride: dark green, calcium: light green, carbon: black, and oxygen: red.

TOC graphic

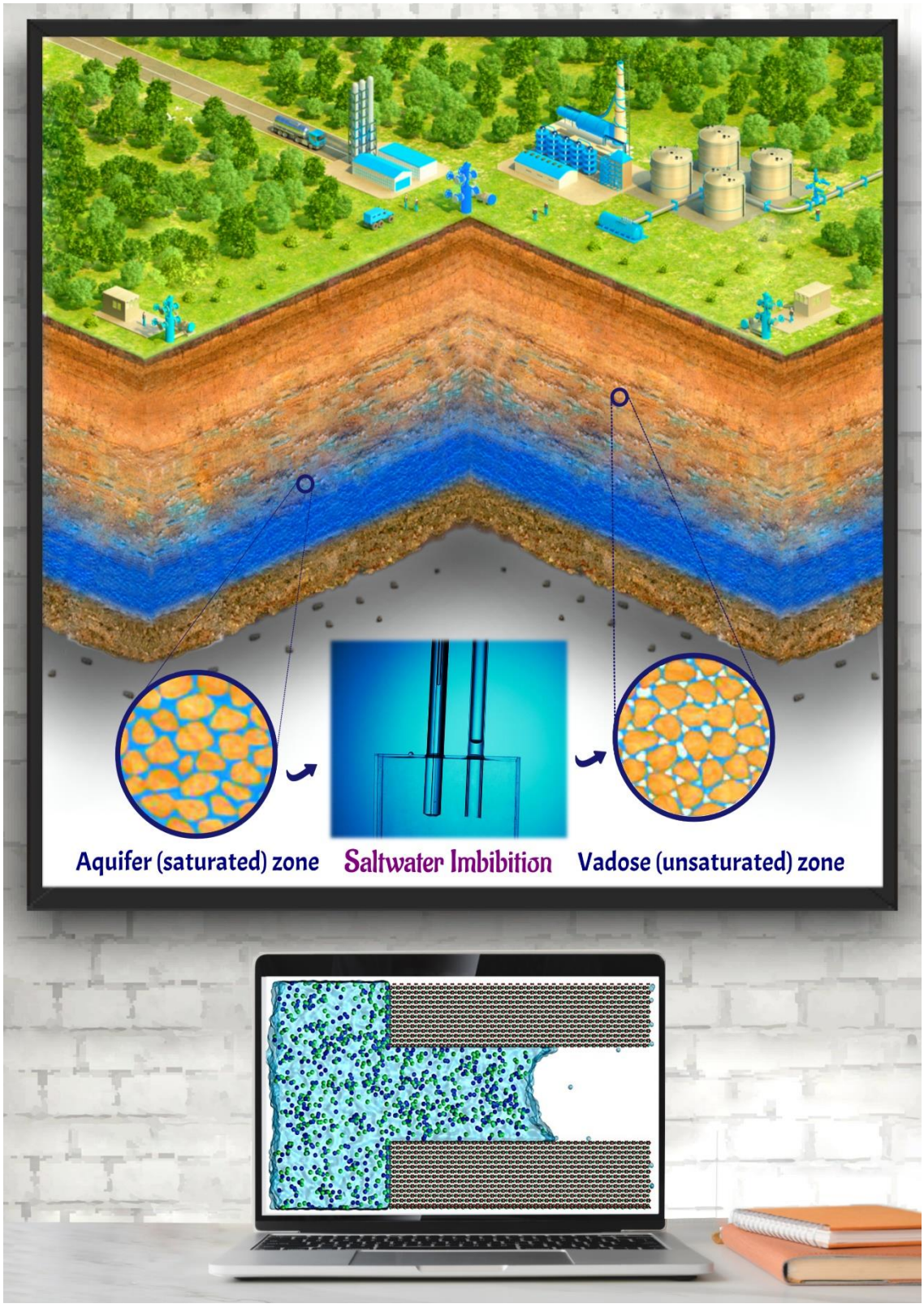
Aquifer (saturated) zone
Saltwater Imbibition
Vadose (unsaturated) zone